IOTA Working Group 3 Discussion Start-up paper on EE, R and LBS

Emittance Exchange via Advanced Phase Space Manipulations

Transformative Applications of Advanced Phase Space Manipulations

Over the last decade, Fermilab has pioneered the experimental development of advanced phase space manipulations at the A0 photoinjector test facility. These manipulations include the generation of "flat" beams with high transverse-emittance ratio [1, 2, 3, 4] and the emittance exchange between the horizontal and longitudinal degrees of freedom [5,6]. The beamline used for the latter experiment was also shown to be capable of producing arbitrary-shaped current profile including the production of sub-picosecond bunch trains with variable spacing as needed to produce, e.g., tunable coherent radiation [7,8]. The combination of these two manipulations could enable the arbitrary repartitioning of emittances between the three degrees of freedom [9,10]. Given the local expertise, this type of experiments will be resumed at ASTA with the end goal of pushing their limits to new frontiers and possibly utilizing these phase-space-manipulation concepts to advance the performances of accelerator-based light sources or new acceleration concepts.

Advanced phase space transformation techniques, flat beam generation, emittance exchange (EEX), and temporal pulse shaping could have transformative applications to advanced accelerator science. At ASTA some of these transformations were included in the baseline design (e.g. flat beam in the photoinjector) and will be readily available to the user. Most of the components and expertise required to assemble other phase space manipulation methods, e.g. emittance exchange, are available. The availability of these manipulation techniques to carry out experiments is unique to the ASTA facility and, when combined with the high-repetition rate, could be utilized to investigate, e.g., dynamical effect in plasma-wakefield accelerators.

Flat Beam Transformation

Under normal conditions, the electron beams generated in a photoinjector are round due to the cylindrical symmetry of the photocathode drive-laser as well as the rf acceleration and solenoidal focusing system. Several factors drive the bulk properties of an electron beam, such as space-charge, beam emittance and angular momentum. An electron beam in thermal motion inside a cathode is born into a region with an axial magnetic field ***B***, suddenly acquiring canonical angular momentum. The beam is then brought into a field-free region, and the kinetic angular momentum is removed by a set of three skew-quadrupole magnets. In this process the initially equal emittances are partitioned into unequal emittances ($\gamma\varepsilon_+$, $\gamma\varepsilon_-$), preserving the product: $\gamma\varepsilon_x \times \gamma\varepsilon_y = \gamma\varepsilon_+ \times \gamma\varepsilon_-$; see Figure 1.

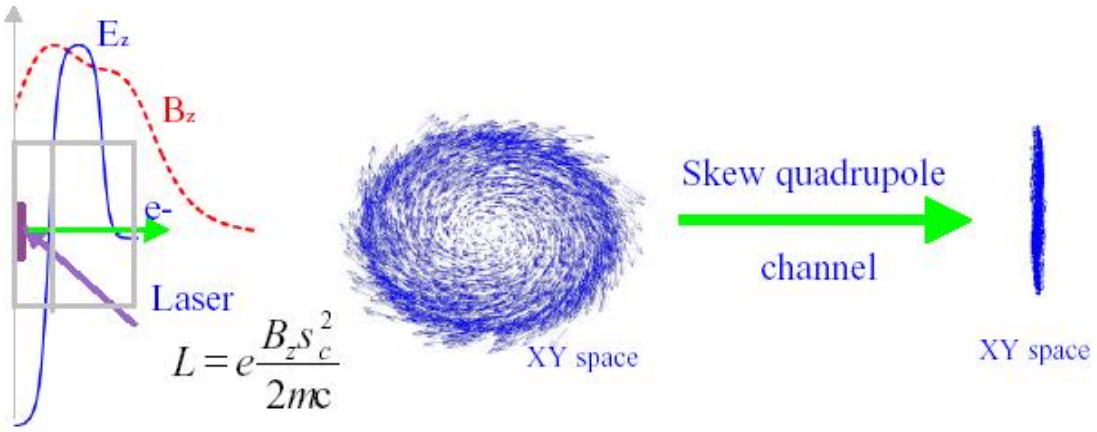

Figure 1: The round-to-flat beam transformation. The beam is produced in an rf gun (left), wherein the axial magnetic field is non-zero, thereby imparting a nonzero canonical angular momentum. Upon exit from the gun and the magnetic field, the canonical angular momentum is converted into kinetic angular momentum (middle). The angular momentum is removed by applying a torque on the beam using a system composed of three skew-quadrupole magnets. The beam is thereby made flat (right).

An unequal partitioning of equal emittances is not possible in a symplectic process; in a symplectic process the emittances in different directions can either remain the same or be exchanged among themselves. The flat-beam technique circumvents this limitation because the process of beam birth in a magnetic field is non-symplectic. The expected flat beam transverse emittances are [11]:

$$\gamma\varepsilon_{\pm} = \left[(\gamma\varepsilon)^2 + (\gamma\Lambda)^2\right]^{1/2} \pm \gamma\Lambda \xrightarrow{\gamma\Lambda >> \gamma\varepsilon} \begin{cases} 2\gamma\Lambda \\ \gamma\varepsilon \\ \dfrac{\varepsilon}{2\Lambda\gamma} \end{cases}$$

where Λ is related to the beam's mean canonical angular momentum. The emittance ratio after the round-to-flat-beam transformation is given by

$$\frac{\varepsilon_+}{\varepsilon_-} \approx \left(\frac{2\gamma\Lambda}{\gamma\varepsilon}\right)^2 = \left(\frac{eB(\sigma_c)^2}{mc\gamma\varepsilon}\right)^2 >> 1,$$

where *e* is the electron charge, *m* is the electron mass, *c* is the speed of light, and σ_c is the transverse rms beam size of the laser on the photocathode. It was recently pointed out that the flat-beam generation from a CAM-dominated beam can be elegantly described using the concept of eigen-emittances; see Ref. [9]. Mathematically, the eigen-emittances are the eigenvalues of the beam matrix. Using this formalism, one can show that the transverse eigen-emittances associated to a CAM-dominated beam are unequal and the RFTB effectively maps the eigen-emittances into the conventional beam emittances (i.e. the determinant of the 2x2 beam matrix sub-blocks associated to each degree of freedom). Therefore the eigen-emittance concept provides a powerful tool for perfecting the settings of a photoinjector. One can then optimize

the performances of the RFTB by insuring the optimum eigen-emittances achieved in the photoinjector are fully transferred into the beam's emittances.

The flat-beam technique was experimentally demonstrated at Fermilab's A0 Photoinjector [4] where an emittance ratio of ~100 was achieved; see Figure 2.

The ASTA photoinjector incorporates a set of three skew-quadrupole magnets, a round-to-flat-beam transformer (RFBT), to possibly convert an incoming magnetized round beam into a flat beam. Furthermore, the solenoidal lenses surrounding the rf gun can be axially moved. The bucking solenoid on the rf-gun was designed to provide a large axial field on the photocathode surface. Therefore, by properly positioning the solenoidal lenses and setting their currents, the axial magnetic field on the photocathode can be tuned from zero to thousands of Gauss. At bunch charge of 1.0 nC and beam energy of 50 MeV, the normalized emittance is optimized around $\varepsilon_{\perp}^{n}$ =2.3 μm [12]. This includes the thermal emittance which is about 0.85 μm for a residual kinetic energy of 0.55 eV from CsTe cathode. Considering the case of a 1000-G axial magnetic field on the photocathode would result in a normalized angular momentum γL= 29.64 μm; then the achievable flat-beam transverse normalized emittances partition is $(\gamma\varepsilon_{-}, \gamma\varepsilon_{+}) \approx$ (0.1, 59.4) μm corresponding to an emittance ratio of ~600. The small emittance will be challenging to measure with the standard multislit method but should be properly diagnosed with the quadrupole scan method. Accelerating these flat beams to 250 MeV while preserving the small emittance will also present interesting challenges and remains to be demonstrated.

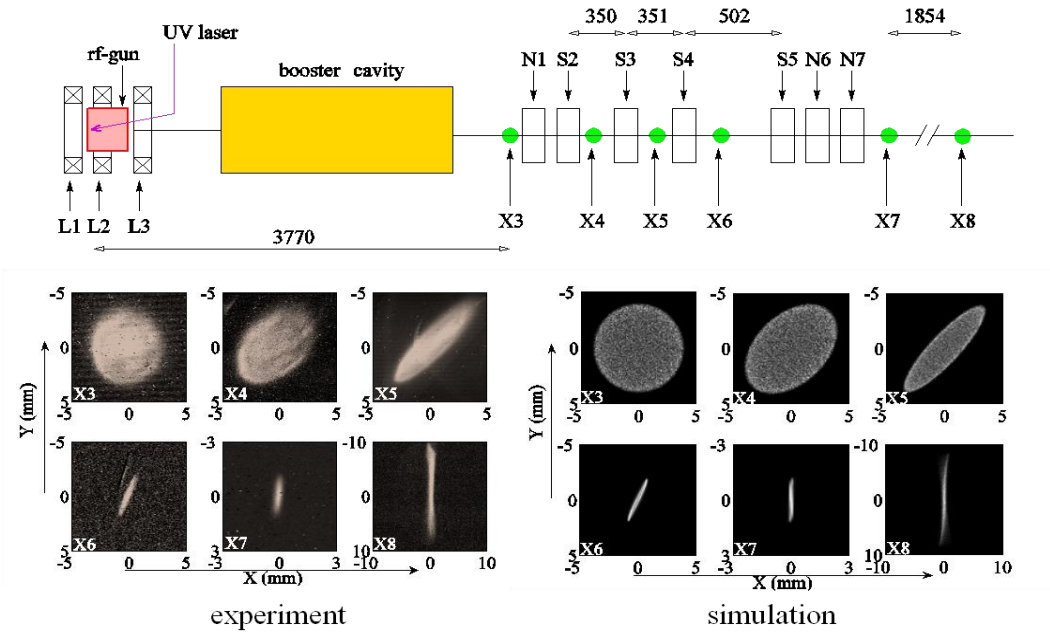

Figure 2: The round-to-flat beam transformation experiment at A0 photoinjector [3]. Top: experimental configuration (the labels "X", "N", "S" respectively represent the locations of diagnostics, normal and skew quadrupole magnets). Bottom: transverse measured (left) and simulated (right) beam density at different axial locations along the accelerator beamline.

We have recently used the concept of eigen-emittances to optimize the generation of flat beams at the ASTA. An example of evolution of eigen-emittance along the ASTA photoinjector for a 3.2-nC beam produced from a photocathode immersed in an axial magnetic field $B \simeq 800$ G appears in Figure 3 (left plot). The achieved beam parameters for the flat- and round-beam scenarios are summarized in Figure 3 (right table). This example confirms that the four-dimensional emittance achieved for round and flat beams are comparable when the beamline settings are adequately optimized. In this particular case, a transverse emittance ratio of 334 was simulated. The optimizations were carried using a Pareto-based multi-objective optimizer with main objectives of: (1) minimizing the four-dimensional emittance and (2) maximizing the eigen-emittance ratio. The conversion of these eigen-emittances to beam's emittance using the skew quadrupole magnets was also confirmed but found to be strongly dependent on the beam's fractional momentum spread.

Finally, compressing the produced flat beam could provide exciting opportunities: compressed flat beam can be used for image charge undulators or beam-driven acceleration techniques employing asymmetric structures. In addition, flat beams could also provide a way to mitigate deleterious effects in a magnetic chicane bunch compressor. Preliminary simulations of the compression of a flat beam with different incoming transverse emittance ratio have been performed [17]. The simulations indicate that the four-dimensional emittance $e_4 \circ \sqrt{e_x e_y}$ degradation is mitigated for flat beams with transverse emittance ratio; see Figure 4. The compression of flat beam at ASTA will be a significant improvement over the experiments carried at the A0 photoinjector.

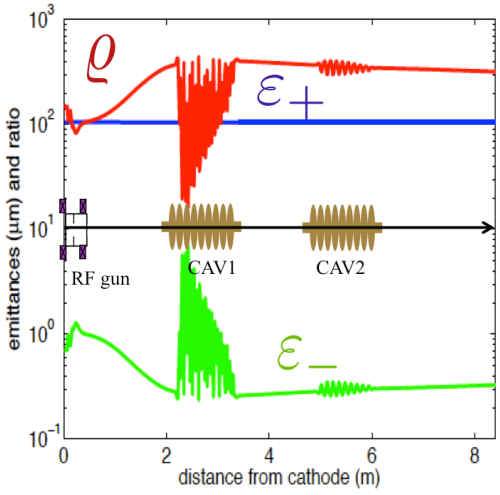

parameter	flat-beam configuration	round-beam configuration	units
Q	3.2	3.2	nC
E	47.18	48.77	MeV
ε_x	105.04	5.43	μm
ε_y	0.31	5.44	μm
ε_{4D}	5.53	5.44	μm
ρ	$\simeq 334$	$\simeq 1$	–

Figure 3: Evolution of eigen emittances (green and red trace) and their ratio (red trace) along the photoinjector beamline (left) and simulated performance of the ASTA photoinjector for the flat- and round-beam configurations (right).

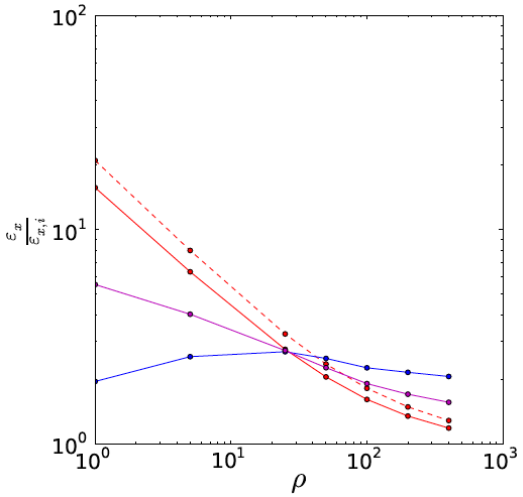

Figure 4: Transverse emittances dilution as a function of incoming flat-beam emittance ratio ($r \equiv \varepsilon_{x,i} / \varepsilon_{y,i}$) through the bunch compressor (BC1) of the ASTA photoinjector. The bending-plane (horizontal) emittance dilution (red traces—correspond to the ratio of final over initial horizontal emittances) is simulated with CSRTrack (dashed line) and IMPACT-Z (solid line). The vertical (blue trace) and four-dimensional ($\varepsilon_4 \equiv \sqrt{\varepsilon_x \varepsilon_y}$, magenta trace) emittance dilutions are obtained from IMPACT-Z simulation. The bunch charge is 3.2 nC [17].

The first-beam configuration of the ASTA photoinjector will readily include the round-to-flat beam transformation and will therefore support experimental studies pertaining to the compression of flat beams with high transverse-emittance ratio. We especially plan to perform parametric study of transverse and longitudinal phase space degradation as function of incoming beam flatness.

Transverse-to-Longitudinal Phase Space Exchange

Over the last decade beamlines capable of exchanging the transverse and longitudinal phase space coordinates have emerged. Typically such beamlines are composed of a deflecting cavity operating on the TM_{110} mode flanked by two dispersive sections. Such a beamline can serve as a phase space exchanger provided the conditions [5]

$$D_+ = \begin{pmatrix} R_{11,+} & R_{12,+} \\ R_{21,+} & R_{22,+} \end{pmatrix} D_- \text{ , and } k = -\frac{1}{\eta_-},$$

are verified. Here the + and - signs refer to values associated to respectively the downstream and upstream dispersive sections, $D \equiv (\eta, d\eta/ds)$ is the dispersion vector, R_{ij} are the usual transport matrix elements, and k is the TDC normalized deflecting strength.

The simplest implementation devised to date is the "double-dogleg configuration" where the two dispersive sections upstream and downstream of the deflecting cavity are simple doglegs each composed of two dipoles; see Figure 5. When this condition is fulfilled and under the thin lens approximation, the horizontal and longitudinal phase space coordinates *(x,x',z,δ)* before and after the EEX are related via

$$\begin{pmatrix} x \\ x' \\ z \\ d \end{pmatrix}_{out} = \begin{pmatrix} 0 & 0 & \frac{L+s}{aL} & aS \\ 0 & 0 & \frac{1}{aL} & a \\ a & aS & 0 & 0 \\ \frac{1}{aL} & \frac{L+s}{aL} & 0 & 0 \end{pmatrix} \begin{pmatrix} x \\ x' \\ z \\ d \end{pmatrix}_{in},$$

where the geometric parameters are introduce in Fig 5. The block anti-diagonal form of this matrix results in an exchange of phase-space coordinates between the horizontal and longitudinal phase spaces. As a consequence the corresponding emittances are also exchanged. It should be noted that other beamline configurations are also capable of exchanging the transverse and longitudinal phase space an alternative approach using a chicane-like configuration is investigated in Ref. [18].

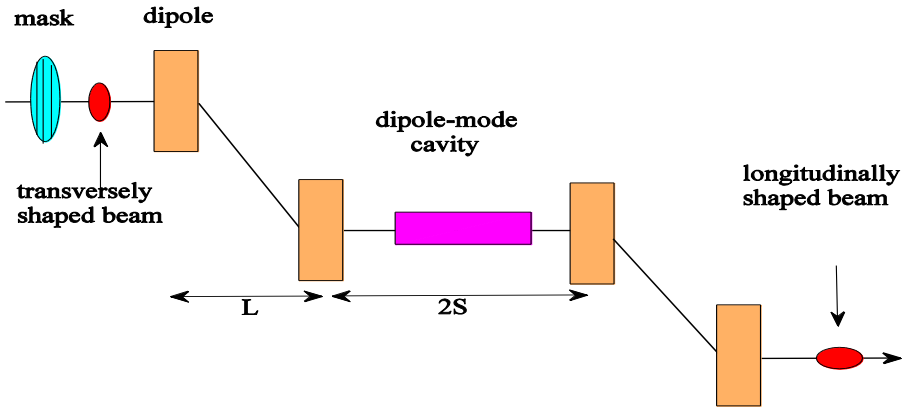

Figure 5: Overview of the double-dogleg transverse-to-longitudinal phase-space-exchanging beamline.

Since this beamline exchanges the phase space coordinates, it also swaps the longitudinal and horizontal emittances. In fact this was the initial motivation for developing this class of beamlines [13]. A proof-of-principle experiment demonstrating the exchange of transverse and longitudinal emittances was carried at the A0 photoinjector [6]. It was later realized that this phase space exchange beamline could also be used as a bunch-current shaper [14] and proof-of-principle

experiment was carried at the A0 photoinjector; see Figure 6. A byproduct of this experiment was the generation of narrowband THz coherent transition radiation. The radiation was shown to have a 20-25 % FWHM relative bandwidth and was tunable over the 0.4-0.9 THz range. These experiments were limited by the mask used to produce a transversely-segmented beam (the mask was indeed optimized to measure the beam emittance). At the A0 photoinjector, the deflecting cavity used was a LN2-cooled normal conducting cavity composed of five elliptical cells following the design of a superconducting cavity developed for kaon separation [15].

We plan on continuing phase space exchange experiments at ASTA. Several avenues to improve over the series of experiments performed at the A0 photoinjector are under consideration. The overarching goals of this "second generation" phase space exchange experiments are:

1. To improve the performance of the first generation phase space exchange experiment, and
2. To find beamline configurations that would be more practical, e.g., that do not offset the beam's direction so that manipulated beams could be sent to the high-energy area and be used to support experiments.

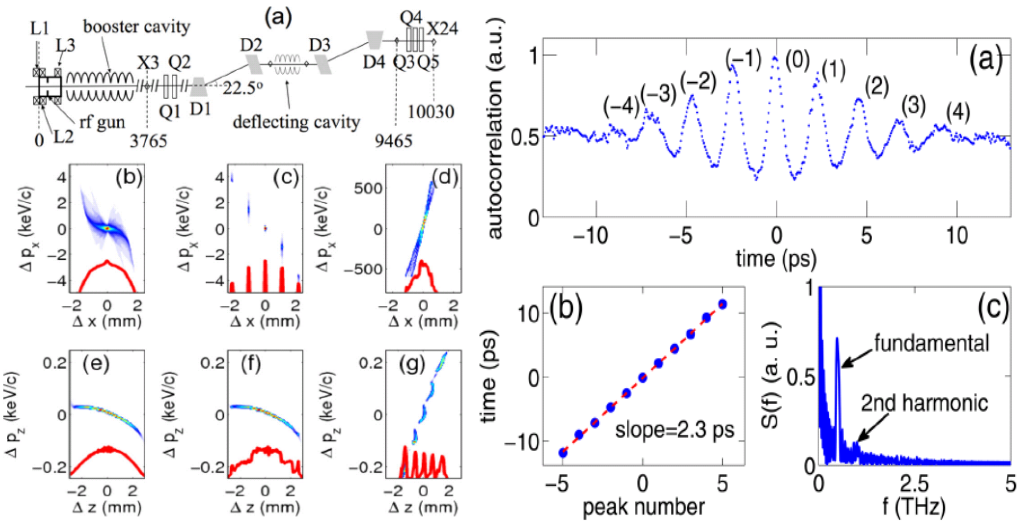

Figure 6: Left figures: (a) experimental configuration and simulated transverse (b,c,d) and longitudinal (e,f,g) phase spaces before (b,e) and after (c,f) the multi-slit mask and downstream (d,g) of the emittance-exchanger beamline. Right figure: typical autocorrelation of transition radiation (a) and corresponding peak separation (b) and frequency analysis (c).

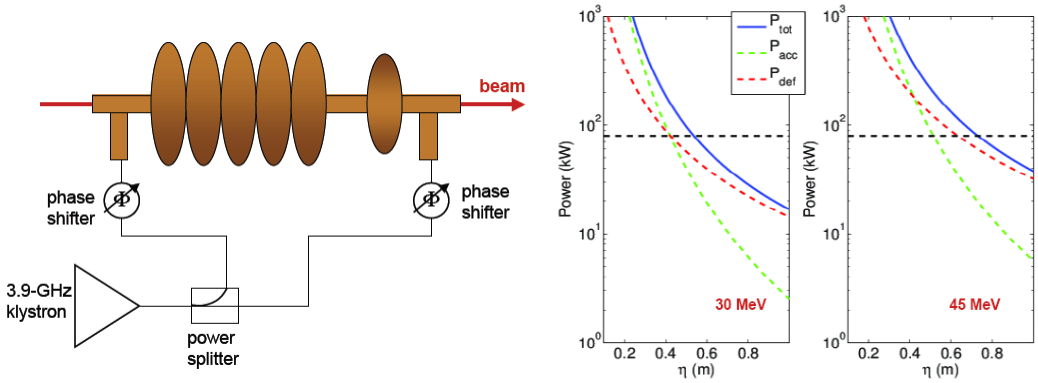

Figure 7: The "thin-lens" deflecting cavity consisting of a five-cell TM110 cavity followed by a single-cell TM010 cavity (left). Requirements on klystron power for ideal longitudinal to transverse phase space exchange as a function of the dispersion value at the cavity location. The calculations are performed for a 3.9-GHz klystron feeding an LN2-cooled system. The horizontal black line corresponds to the maximum power available from the available klystron.

Item (1) consists in improving the diagnostics downstream of the phase space exchanger beamline (the A0 experiment did not have any viable longitudinal phase space diagnostics which precluded a direct measurement of the final longitudinal emittance) and possibly considering an "hybrid" deflecting cavity that will also have a 6th cell operating on the TM_{010} mode. The latter improvement was shown to cancel some aberration associated the realistic (and not thin lens model) of deflecting cavities [16]. The current 3.9-GHz rf system should be able to drive such a hybrid cavity provided the dispersion at the cavity is close to 0.8 m (for a 50 MeV beam); see Figure 7. One option would consist in installing a double-dogleg beamline in the 50 MeV experimental area; see Figure 8. However due to the limited 3.9-GHz klystron power (80 kW), the use of a LN2-cooled deflecting cavity forces us to increase the dispersion in order to lessen the deflecting strength required for full phase space exchange. In the current layout, the dipole magnets in each dogleg are separated by 1.07 m and the distance between the two central dipole magnets is 1.99 m. Each dipole bends the beam by 22.5° while each dogleg generates a dispersion of 44 cm. The beamline was modeled using General Particle Tracer with 3D space-charge effects included for a 250 pC and 50 MeV electron bunch. The design is in essence very similar to the setup used at the A0 photoinjector but would include better diagnostics. In addition it could support experiments aiming at repartitioning the emittances within the three degrees of freedom. In such experiments, the flat beam transform would be used to create a flat incoming beam and the phase space exchange would exchange the horizontal and longitudinal emittances. This versatility would allow for parametric studies of the phase space exchange mechanism. Finally the beamline could also support more advanced current shaping technique. Using triangular mask (or shaping the transverse profile of the laser on the photocathode) could be used to produce ramped bunches which have extremely important applications in beam driven wakefield acceleration technique as they enhance the transformer ratio.

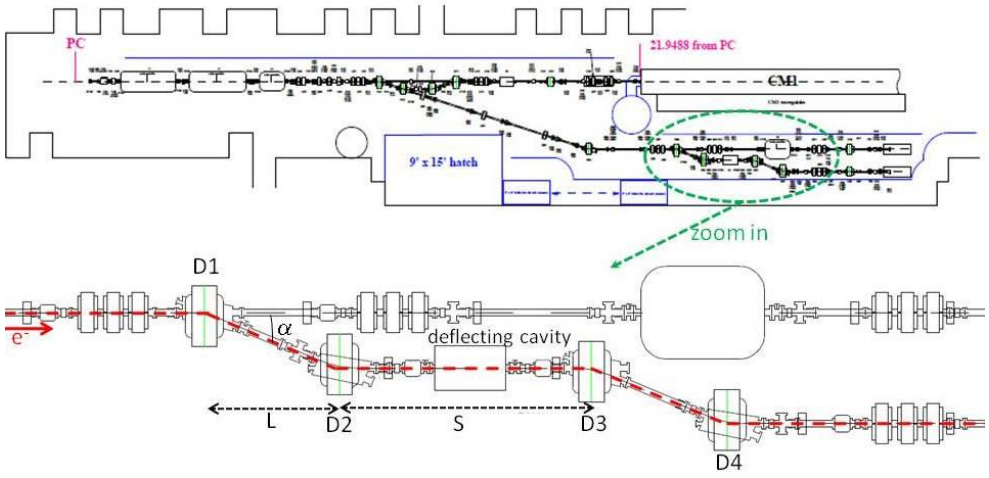

Figure 8: The NML injector and double dogleg beamline for the transverse-to-longitudinal phase space exchange.

Beside the double-dogleg beamline, other configurations are also possible, such as the magnetic chicane with quadrupoles inserted between the dipole. This latter setup has the main advantage of not translating the beam direction and could be a more suitable configuration for a higher energy phase space exchanger. It could also open the exploration of tradeoff between dispersion and deflecting strength. Numerical simulations are currently underway to explore possible layouts at ASTA and examples of preliminary results are displayed in Figure 9. In the latter it was demonstrated via numerical simulation that the double-dogleg and chicane-line configurations have very similar performances though their optical lattice has substantial difference (the double-dogleg beamline has a stronger compression ratio than the chicane-like configuration).

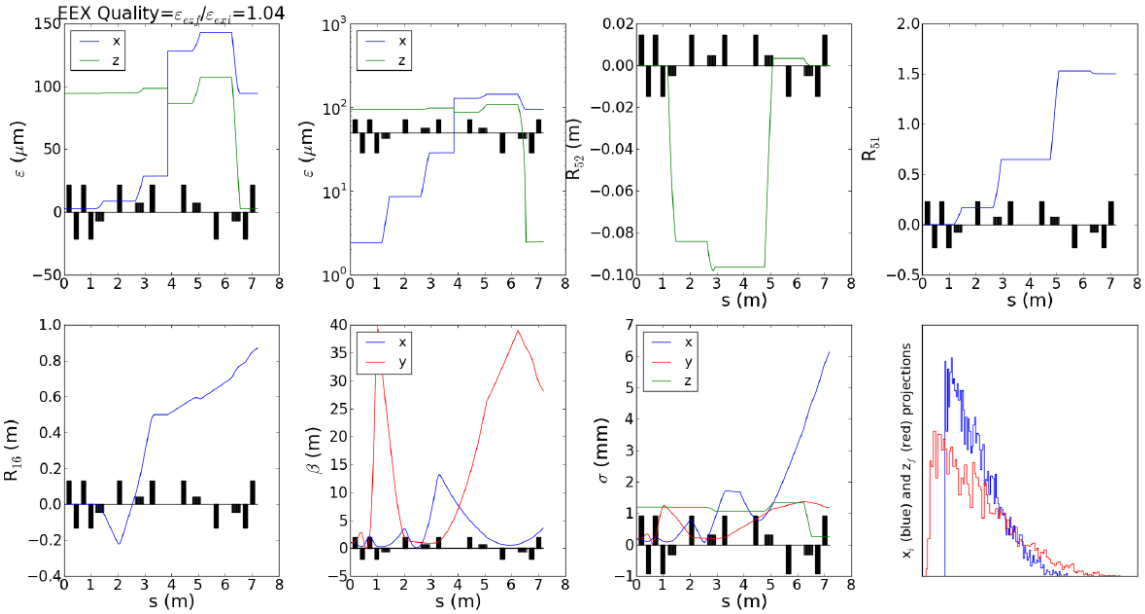

Figure 9: Horizontal (blue trace) and longitudinal (green trace) emittance evolution along the chicane-like emittance exchanger (top row, first two plots). Evolution of cumulated transfer matrix elements (top row last two plots and bottom left plot), beta functions (2nd plot on bottom row). Horizontal (blue trace), vertical (red trace) and longitudinal (green trace) beam rms size evolution (second row 3rd plot). Left plot on second row show the transformation of an incoming linearly ramped horizontal profile downstream of the exchanger to illustrate the production of linear-ramped current distribution [18].

Transverse-to-Longitudinal Phase Space Exchange Downstream of Cryomodule(s)

The chicane-type configuration described in the previous section could form the basis for a phase space exchange beamline downstream of the ASTA cryomodule(s). The available real-estate would also enable tests of the double emittance exchange beamline suggested by A. Zholents. In this configuration, two phase-space exchangers are placed back to back and separated by an appropriate optical lattice; see Figure 10. Locating a mask between the two exchangers would enable beam shaping discussed earlier without, in principle, exchanging the horizontal and longitudinal emittance (an initially transversely round beam would have its final transverse emittances preserved).

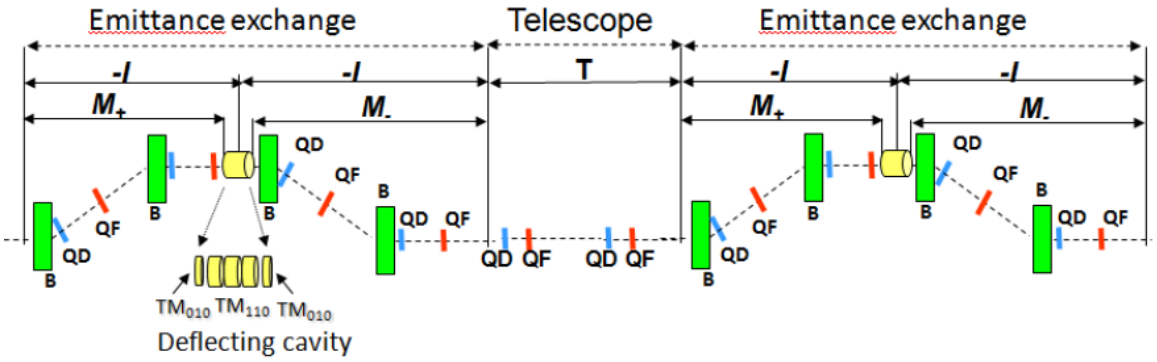

Figure 10: A possible configuration for a double phase space exchange [16].

This configuration could also serve has a bunch compressor that does not require the impression of a correlated energy spread on the incoming beam as needed in a conventional magnetic compressor. In such a scheme, the section between the two exchangers would demagnify the beam horizontally resulting in a shorter bunch length after phase-space exchange in the exchanger. This manipulation has been included in a variant of the compressed harmonic generation (CHG) scheme for seeding short-wavelength free-electron lasers and discussed elsewhere in this proposal.

The overall advantage of such a “double phase space exchanger” configuration compared to a single phase space exchanger is that it leaves the transverse emittances unaffected (under linear optics). This bunch compressor could also be used for frequency up-conversion of the energy modulation provide by the laser interaction with electron beam, and thus can possibly seeding a free-electron laser at a significantly higher harmonics; or it can also be used to do frequency down-conversion for generation of THz radiation.

The design of such a double EEX beamline would require a detailed study as our preliminary investigation indicate that second-order effects are detrimental and need to be mitigated by inclusion of sextupoles. On another hand, from an order-of-magnitude analysis, LN2-cooled cavities would put a high power demands (several MW) on the klystrons. Thus it is natural to consider a SRF system operating at 3.9 GHz similar to the system developed at Fermilab for kaon separation and longitudinal phase space linearization of the FLASH accelerator at DESY. A possible configuration using the 3.9-GHz deflecting and accelerating mode cavities developed at Fermilab is diagrammed in Figure 11, other solution based on other types of cavities are also being considered.

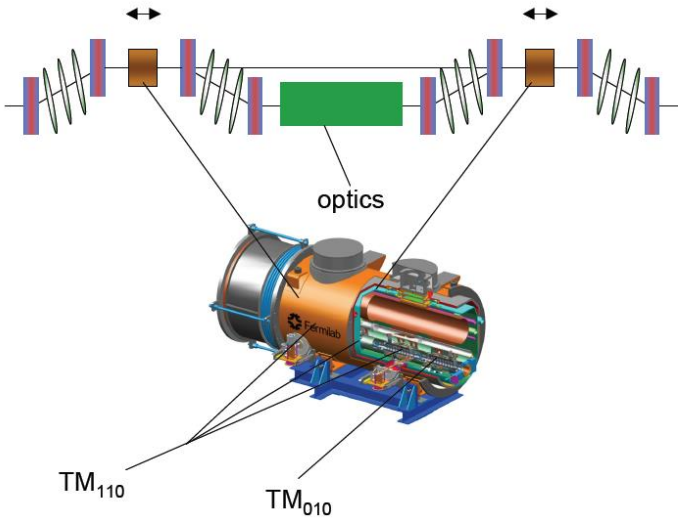

Figure 11: A possible configuration for a 3.9 GHz deflecting/accelerating hybrid SRF structure for a double phase space exchanger in the high energy beamline of ASTA.

References

[1] D. A. Edwards, et al., "Status of the flat electron-beam production,” Proceedings of the 2001 Particle Accelerator Conference, Chicago, p. 73 (2001).

[2] Y.-E Sun, "Angular-momentum-dominated electron beams and flat-beam generation,” PhD Dissertation, University of Chicago (May 2005).

[3] Y.-E Sun et al., Phys. Rev. ST Accel. Beams 7, 123501 (2004).

[4] P. Piot, Y.-E. Sun, and K.-J. Kim, Phys. Rev. ST Accel. Beams 9, 031001 (2006).

[5] T. Koeth, PhD Dissertation, "An Observation of a Transverse to Longitudinal Emittance Exchange at the Fermilab A0 Photoinjector," Rutgers University (May 2009).

[6] J. Ruan, et al., Phys. Rev. Lett. 106, 244801 (2011).

[7] Y.-E Sun et al., Phys. Rev. Lett. 105, 234801 (2010).

[8] P. Piot, et al., Appl. Phys. Lett. 98, 261501 (2011).
[9] N. Yampolski, et al., "Controlling Electron-Beam Emittance Partitioning for Future X-Ray Light Sources," preprint arXiv: 1010.1558 (2010).
[10] P. Emma, Z. Huang, K.-J. Kim, and P. Piot, Phys. Rev. ST Accel. Beams 9, 100702 (2006).
[11] K.-J. Kim, Phys. Rev. ST Accel. Beams 6, 104002 (2003).
[12] P. Piot, Proc. IPAC'10, Kyoto, Japan, (23-28 May 2010), p. 4316.
[13] M. Cornacchia and P. Emma, Phys. Rev. ST Accel. Beams 5, 084001 (2002).
[14] P. Piot, et al., Phys. Rev. ST Accel. Beams 14, 022801 (2011).
[15] M. McAshan and R. Wanzenberg, report FERMILAB-TM-2144 (2001).
[16] A. A. Zholents and M. S. Zolotorev, "A New Type of Bunch Compressor and Seeding of a Short Wave Length Coherent Radiation," report ANL/APS/LS-327 (2011).
[17] C. Prokop, P. Piot, B. Carlsten, M. Church, "Beam dynamics performances and applications of a low-energy electron-beam magnetic bunch compressor," Nucl Instrum. A 716, pp. 17-28 (2013).
[18] C. Prokop, P. Piot, and B. E. Carlsten, Proc. IPAC13, Shanchai, Japan (12-17 May 2013), 3103 (2013).

Novel Radiation Sources

High-Brightness X-ray Channeling Radiation Source

The quest for a short-wavelength compact light source has been driven by applications ranging from fundamental science to homeland security. Recently, Vanderbilt and Northern Illinois University received funding to work on the development of a compact X-ray radiation source. The proposal aims at producing X-rays using a 50 MeV electron beam. A proof-of-principle experiment is foreseen in the ASTA photoinjector area. This project aims at producing X-rays at 80 KeV with high-average spectral brilliance. The proposal leverages on the ASTA's pulse-train format capabilities. Conversely, the possibility of an operating field-emission cathode in the ASTA rf gun would provide a bunch train with a 1.3-GHz intra-bunch frequency. Such high-repetition rate train could be used to, e.g., explore high-order-mode excitation in the ASTA superconducting linac in a new regime. In addition, the exquisitely small emittance projected from the field-emission source will move RF-accelerator science into a regime where it has never played a role before. New diagnostics will be needed even to explore this region, and new effects will probably be discovered. Extension from a single field-emitter to an array will increase the total current, and used together with the beam-manipulation developments discussed in the following section may play a role in the development of coherent light sources. Thus, as an extra benefit, the channeling-radiation project will advance the basic objective of ASTA as an accelerator research tool. A major advantage of ASTA is its capability of supporting an X-ray source with high-average spectral brilliance. This section is based on the proposed concept detailed in Ref. [1].

Introduction: Channeling Radiation as an Ultra-bright X-ray Source

In a crystal, the ions in each crystal plane form a sheet of positive charge. When a relativistic electron travels through the crystal parallel to the crystal plane, Lorentz contraction increases the charge density by the factor γ and the electron oscillates about the crystal plane in quantum states normal to the plane, as depicted in Figure 1. Radiation from transitions between the quantum states is called channeling radiation. Channeling radiation was predicted theoretically by Kumakhov [2] in 1974, and experimentally observed by Terhune and Pantell [3] in 1975. Since then, there has been extensive theoretical and experimental investigation of channeling raiation, and theory and experiment are in good agreement.

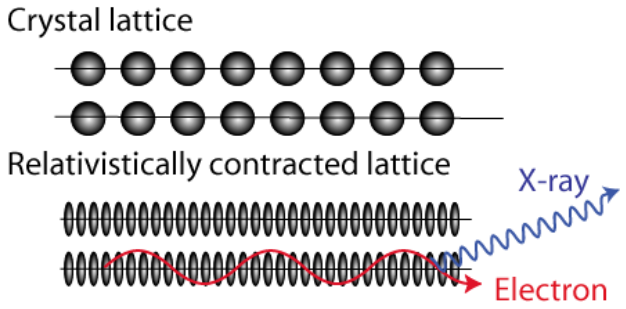

Figure 1: Mechanism of channeling radiation production [1].

The transverse forces experienced by an electron traveling along a crystal plane are comparable to those in a 10^4-T magnetic undulator or a 1-TW laser undulator focused to a 10-μm spot. The equivalent "undulator period" is on the order of 0.1 μm. The coherence length of the crystal "undulator" is limited by scattering to the order of 1 μm, so the effective number of "undulator periods" in channeling radiation is on the order of 10. The photon yield is more than 10 photons per electron at high energy (GeV), but on the order of 10^{-4} photons per electron in the X-ray region [4]. The channeling-radiation peaks are typically an order of magnitude above the bremsstrahlung background [5]. The advantages of a channeling radiation source are clear. Compared with a conventional undulator, channeling radiation requires only a 50 MeV electron beam, rather than a 10-GeV beam to reach the hard X-ray region. Compared with a laser undulator, a channeling radiation source comprises a small diamond chip rather than a complex laser system circulating a kilowatt of laser power.

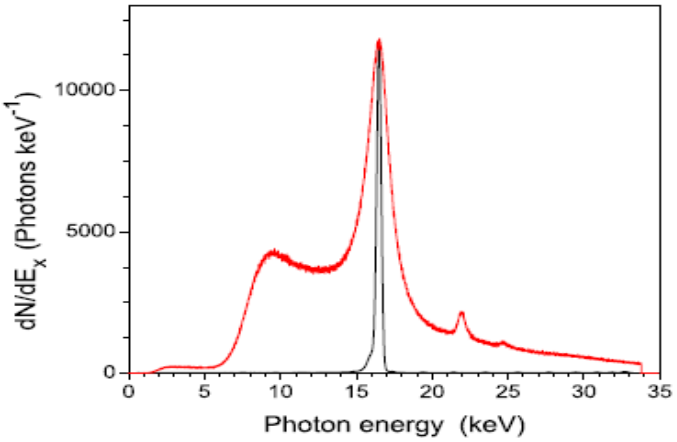

Figure 2: Observed spectrum of channeling radiation for transitions in (110) plane of diamond crystal at an electron energy of 14.6 MeV. Red: natural spectrum; black, monochromatized by Bragg reflection to remove the wings of the CR line and the Bremsstrahlung background [6].

For electrons channeling in diamond, the best available measurements are those of Azadegan [6]. A typical channeling radiation spectrum is illustrated in Figure 2. The radiation is forward directed in a cone of angle $1/\gamma$, and Doppler shifted by the factor 2γ. Including the Lorentz contraction of the crystal lattice, the photon energy scales roughly as $\gamma^{1.7}$, and spans the X-ray and gamma ray regions. For the $1 \rightarrow 0$ transition in (110) diamond, the photon energy may be tuned from 10 to 80 keV by varying the electron energy as depicted in Figure 3. For a 30-MeV electron incident on a 42.5-micron thick diamond crystal, the yield on the $1 \rightarrow 0$ transition corresponds to about 0.028 photons-steradian-keV in a line 3-keV wide centered near 56 keV [6]. In conventional units, this corresponds to 10^{-9} photons-mrad^2-0.1% bandwidth per electron.

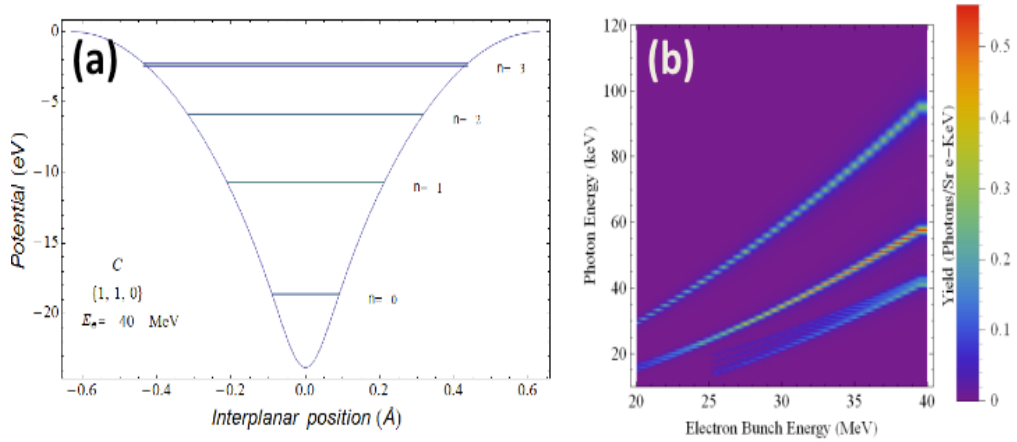

Figure 3: Simulated bounded states (horizontal line) and potential for the case of a 40-MeV beam channeling in a (1,1,0) diamond structure (a) and calculated yield as function of incoming electron bunch energy available in the ASTA photoinjector. The 3 traces in the density plot (b) correspond to the three allowed transitions between bounded states [17].

The spectral brilliance of the X-radiation depends on how tightly the electron beam can be focused, and this depends on the emittance of the beam. At the radiation source ELBE, in Dresden, a high-intensity channeling radiation source has been developed using a high-brightness electron beam incident on a diamond crystal [4]. Diamond is the best material for this application owing to its high thermal conductivity [7]. The normalized emittance of the beam after aperturing was 3 µm rms at an average current of 100 µA [8], which corresponds to a peak brightness on the order of 10^9 A/m^2-sterad. The beam was focused to a mm-size spot on the diamond. As much as 10^{11} photons/s were obtained in a 10% bandwidth, which corresponds roughly to an average spectral brilliance on the order of 10^6 photons/s-mm^2-mrad^2-0.1% bandwidth.

The innovation being pursued by the Vanderbilt/NIU group is to use a single field-emitting tip as the current source, in place of the gridded thermionic gun used at ELBE. Simulations of a single-tip field emitter yield a normalized emittance of 1.3 nm [9], which is an improvement of three orders of magnitude over the ELBE thermionic gun. In experiments at Vanderbilt, we have observed more than 10 µA average current from a single field-emitting tip [10] with brightness approaching the quantum limit [11]. The current was limited by damage to the anode, which was in close proximity. The ultimate performance of diamond tips has yet to be determined. By using a single tip it may be possible to improve the transverse brightness of the electron beam by as much as six orders of magnitude, with a corresponding improvement of the spectral brilliance of the X-ray beam. The absolute emittance of the beam from a single tip, extrapolated to 30 MeV, is ~40 pm. If we focus this at the critical angle for channeling radiation in diamond (about 1 mrad), we get a spot diameter of 40 nm; the spectral brilliance of the X-ray beam is then 10^{12} photons/s-mm^2-mrad^2-0.1% bandwidth at an average current of 200 nA.

Production of X-rays at ASTA: Challenges and Methods

The beam must be accelerated to high energy (~50 MeV) to create hard X-rays. At ASTA, the first-stage acceleration will occur in the rf-gun to energies up to 4-5 MeV and further acceleration to 50 MeV will happen in CAV1 and CAV2 cavities. We currently envision the field-emitter cathode to be mounted on the tip of the inner conductor of a coaxial line. The coaxial line will be driven by 1.3 and 3.9-GHz signals with solid-state amplifiers to bias the gate electrode and gate the field emission over duration shorter than the rf gun's fundamental period. Calculations indicate that such a biasing scheme will generate bunches with duration of approximately 20 ps [12]. Preserving the ultra-low transverse emittances produced by the tip after subsequent acceleration and manipulation will be challenging. Chromatic aberrations due to energy spread in the beam; emittance dilution due to nonlinearity in the rf fields, geometric aberrations in the electron beam transport lines, and collective effects can be mitigated according to start-to-end numerical simulations [13]. Numerical simulations performed for the ASTA configuration are summarized in Figures 4 and 5. The simulated electron-beam parameters represent two orders of magnitude increase in electron beam quality. Other degrading effects which to date have been unnoticed, may also become important. One concern, for instance, is the extent to which Coulomb collisions at low energies (Boersch effect) will contribute to phase-space dilution [14].

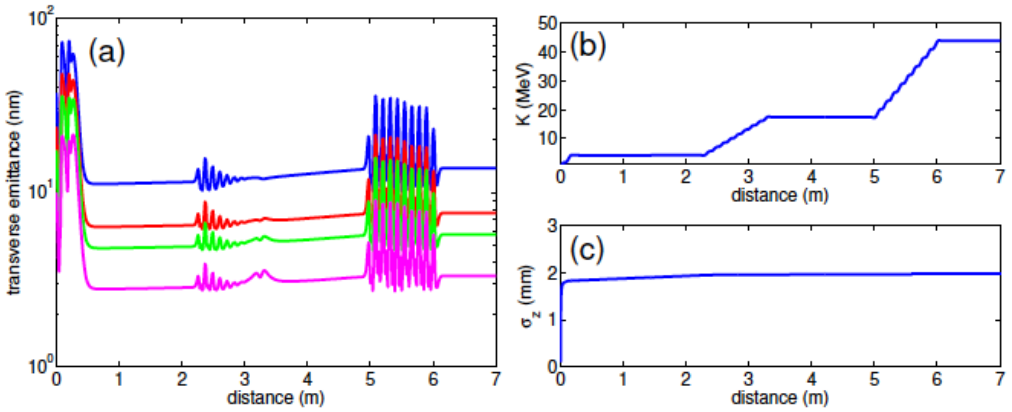

Figure 4: Transverse emittance (a), kinetic energy (b) and bunch length (c) evolution along the ASTA photoinjector accelerating section [comprising the RF gun (0<z<30 cm), CAV1 (2.2<z<3.2 m) and CAV2 (5<z<6 m)]. The magenta, green, red and blue traces in plot (a) correspond to emittance respectively computed for the 85, 90, 95, and 100-percentile of the particle distribution [13].

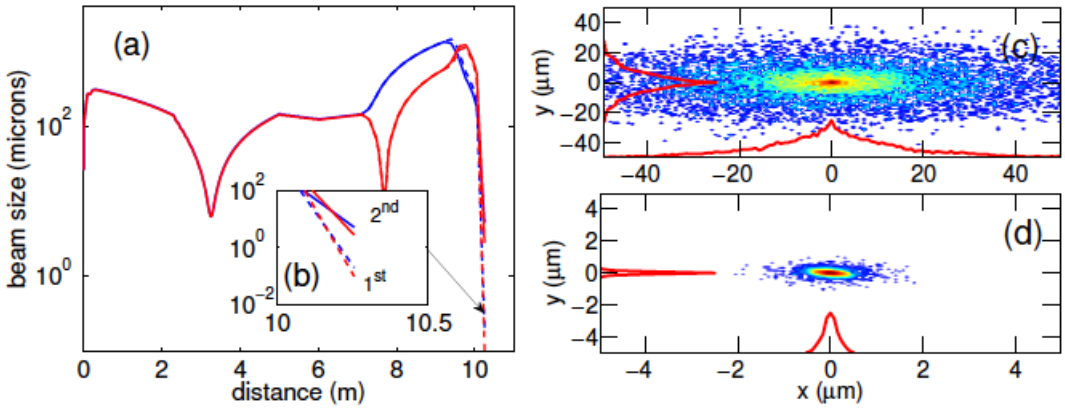

Figure 5: Horizontal (blue) and vertical (red) rms beam size evolution along the ASTA photoinjector beamline up to location of the diamond crystal (a). The solid and dashed line corresponds respectively to second- ("2nd") and first-order "1st") particle-tracking simulations and inset (b) shows the rms beam sizes in the vicinity of the crystal. Density plots (c) and (d) are respectively the beam transverse density at the crystal location obtained from second and first order calculations. The red traces in plots (c) and (d) are the corresponding horizontal and vertical projections [13].

Because the x-rays are produced by the interaction of the electron beam with the crystal, the maximum current of the electron beam is limited by heating of, and radiation damage to, the crystal. Measurements and computations show that for diamond at room temperature the effects of heating are acceptable up to a few mA of beam current, so this will not be a limitation even for cw operation [7]. Measurements show that radiation damage becomes significant above a total beam fluence on the order of a few C per square centimeter. Thus, the 40-nm focal spot is destroyed in about 100 μs. The crystal must be moved at about 1 mm/s, and the crystal is destroyed at the rate of 0.1 square millimeters per hour at 100% duty factor. At the 1-percent duty factor of ASTA, the diamond consumption rate will be much smaller.

Experimental Plans at ASTA

The production of channeling radiation will use the 50 MeV beam produced by ASTA; see Figure 6. We plan to install the channeling radiation crystal downstream of a set of quadrupole magnets and just upstream of the first dipole of a chicane bunch compressor. This configuration will enable us to focus the beam on the crystal and separate the electron beam from the X-rays using the first dipole. In the straight-ahead line we plan on installing the energy-resolved CdTe detector needed to characterize the X-ray radiation.

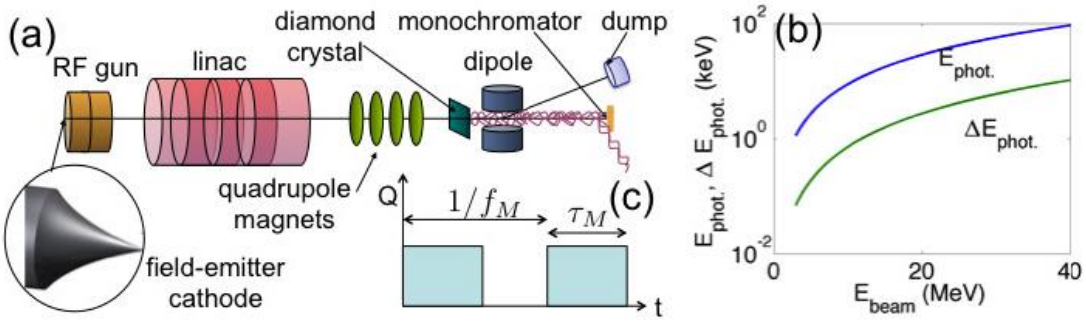

Figure 6: The layout of the X-ray channeling radiation source experiment in the 50 MeV area of ASTA [13].

To minimize the risk, the approach will be staged. First the coaxial cathode holder will be developed and tested at the HBESL facility where the generation of field-emitted bunched beam will be demonstrated. Upon successful completion of this experiment the coaxial-line cathode holder will be installed at the ASTA. Because of the similarities between the HBESL and ASTA rf guns, we expect that the field-emitted cathode holder and associated subsystems developed during the test at HBESL will be integrally reusable without major changes. In parallel and independently from the success of the field-emission source R&D, we will use the nominal electron beam produced via photoemission to gain experience with producing and detecting X-rays from channeling radiation. It is expected that nanometer-level transverse emittance could also be produced by photoemission from the nominal Cesium-Telluride cathode using very small transverse laser spot [15]. Generation and characterization of ultra-low-emittance beams will be attempted during early commissioning of the ASTA photoinjector.

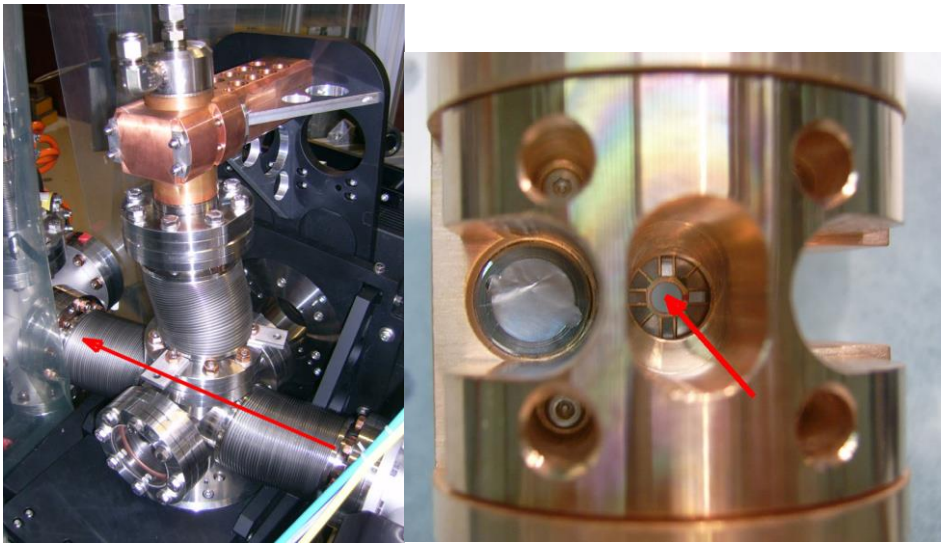

Figure 7: Photograph of the goniometer (left) and cooled crystal holder (right) to be installed in the ASTA photoinjector. The red arrow on the left photograph indicates the

beam direction. The red arrow on the right photograph points to the diamond crystal location.

The goniometer needed to precisely control the orientation of the diamond crystal was provided by collaborators from the Helmoltz-Zentrum Rozendof; see photographs in Figure 7.

Other Spin-off Opportunities

The demonstration of the generation of bunched beam from field emission could find other applications especially since the principle could be applied to a field-emitter array cathode instead of a single-tip field emitter. The latter could produce much higher charge per bunch. For instance, if operated over the full duration of the macropulse, the total number of field-emitted bunches would be 1.3×10^6. Assuming a charge per bunch of 1 pC, this would results in a 1 mC charge within the entire macropulse. This type of unprecedented bunch format could be used to investigate high-order mode excitation in the TESLA cavity or mimic the charge per macropulse anticipated in high-intensity linacs (e.g. Project X) proposal. In addition, the generation and acceleration of electron beams with exquisitely small emittance will extend accelerator technology to a new level. Alternatively a photo-field-emission cathode could be used and attosecond manipulation of the emitted bunches could be anticipated [16] thereby enabling new regimes for planned experiments in advanced acceleration technique or development of novel compact X-ray sources capitalizing on advanced phase space manipulations pioneered at Fermilab.

References

[1] C. Brau, B. Choi, J. Jarvis, J. W. Lewellen and P. Piot, Synchrotron Radiation News, 25: 1-20 (2012); online at http://dx.doi.org/10.1080/08940886.2012.645419.

[2] M. A. Kumakhov, Phys. Lett. A 57, 17 (1976).

[3] R. W. Terhune and R. H. Pantell, Appl. Phys. Lett 30, 265 (1977).

[4] W. Wagner, B. Azadegan, M. Sobiella, J. Steiner, K. Zeil, and J. Pawelke, Nucl. Instrum. Meth. B 266, 327 (2008).

[5] M. A. Kumakhov, International Conference on Charged and Neutral Particles Channeling Phenomena, edited by S. B. Dabagov.

[6] B. Azadegan, Ph.D. thesis, Technischen Universität Dresden, 2007.

[7] C. K. Gary, R. H. Pantell, M. Ozcan, M. A. Piestrup, and D. G. Boyers, J. Appl. Phys. 70, 2995 (1991).

[8] W. Neubert, B. Azadegan, W. Enghardt, K. Heidel, J. Pawelke, W. Wagner, Nucl. Instrum. Meth. B 254, 319 (2006).

[9] C. Brau, Private communication (2011)

[10] J. D. Jarvis, H. L. Andrews, C. A. Brau, B.-K. Choi, J. Davidson, W.-P. Kang, and Y.-M. Wong, J. Vac. Sci. Technol. B 27, 2264 (2009).
[11] J. D. Jarvis, H. L. Andrews, B. Ivanov, C. L. Stewart, N. de Jonge, E. C. Heeres, W.-P. Kang, Y.-M. Wong, J. L. Davidson, and C. A. Brau, J. Appl. Phys. 108, 094322 (2010).
[12] J. W. Lewellen and J. Noonan, Phys. Rev ST Accel. Beams 8, 033502 (2005).
[13] P. Piot, C.A. Brau, W. E. Gabella, B. K. Choi, J. D. Jarvis, J. W. Lewellen, M. Mendenhall, D. Mihalcea, Fermilab-Conf-12-425-APC; Proceedings of the 2012 Advanced Accelerator Concept Workshop (AAC12), Austin TX, June 10-15, 2012.
[14] H. Boersh, Zeit. Physik, 139, 115 (1954).
[15] R. K. Li, K. G. Roberts, C. M. Scoby, H. To, and P. Musumeci, Phys. Rev. ST Accel. Beams 15, 090702 (2012).
[16] M. Krueger, M. Schenk, and P. Hommelhoff, Nature 475, 77 (2011).
[17] B. Blomberg, C. Brau, B. Choi, W. Gabella, M. Medenhall, D. Mihalcea, H. Panunganti, P. Piot, W. Wagner, “Channeling radiation with low-energy electron beams: experimental plans and status at Fermilab,” Proceedings of the 2013 Free-Electron Laser Conference (FEL-2013).